International Journal of Plasticity 152 (2022) 103247

Contents lists available at ScienceDirect

International Journal of Plasticity

journal homepage: www.elsevier.com/locate/ijplas

In situ EBSD/DIC-based investigation of deformation and fracture mechanism in FCC- and $L1_2$-structured FeCoNiV high-entropy alloys

Zhenhua Ye [a], Chuanwei Li [a,*], Mengyao Zheng [a], Xinyu Zhang [a], Xudong Yang [a], Jianfeng Gu [a,b,*]

[a] Institute of Materials Modification and Modelling, School of Materials Science and Engineering, Shanghai Jiao Tong University, Shanghai 200240, China

[b] Shanghai Key Laboratory of Materials Laser Processing and Modification, Shanghai Jiao Tong University, Shanghai 200240, China

ARTICLE INFO

Keywords:
In situ EBSD and DIC
$L1_2$ structure
High-entropy alloy
Deformation behavior
Fracture mechanism

ABSTRACT

This study investigated the plastic deformation behavior of a polycrystalline $L1_2$-structured FeCoNiV high-entropy alloy (HEA) using in situ electron backscatter diffraction (EBSD) and digital image correlation (DIC) methods. The different deformation mechanisms in two HEAs, which affected their mechanical performance, were explored using a face-centered cubic (FCC)-structured sample for comparison. Using slip traces and lattice rotation path analysis, {111}<110> slip systems were found to be activated in the $L1_2$-structured FeCoNiV HEA. In addition, a lower average lattice rotation rate was estimated for this sample compared to that of the FCC specimen; this macroscopically verified the existence of additional obstacles to dislocation slip caused by the ordered structure during plastic deformation, and was found to contribute to the high strength of the $L1_2$-structured FeCoNiV HEA. Furthermore, these additional obstacles blocked the formation of deformed substructures in the $L1_2$-structured sample and aggravated the intergranular incompatibility, which enabled crack initiation at the grain boundaries. These findings are important for understanding the deformation behavior and fracture mechanism in $L1_2$-structured HEAs and for designing new high-performance ordered HEAs.

1. Introduction

High-entropy alloys (HEAs) are new alloy systems proposed by Yeh and Cantor that employ a mixture of at least four principal elements in an equimolar or near-equimolar ratio, and have attracted tremendous scientific attention (Cantor et al., 2004; Ding et al., 2019; Shi et al., 2021; Yeh et al., 2004). In addition, a noteworthy combination of high strength and decent ductility has been achieved by precipitation-strengthening HEAs, especially in systems with $L1_2$ as the precipitation phase (He et al., 2016; Jo et al., 2019; Liu et al., 2016; Tong et al., 2019; Yang et al., 2018; Zhao et al., 2017). Moreover, researchers have expended considerable effort to explain the deformation behavior and strengthening mechanism of HEAs, which have revealed the significance of the coherent $L1_2$ phase (He et al., 2021; Li et al., 2020). However, little attention has been paid to the deformation of the $L1_2$ phase in HEAs, although the ordered structure of HEAs has been recently examined (Qiu et al., 2017; Rogal et al., 2017; Wang et al., 2019). Previous studies have shown that

* Corresponding authors
E-mail addresses: li-chuanwei@sjtu.edu.cn (C. Li), gujf@sjtu.edu.cn (J. Gu).

https://doi.org/10.1016/j.ijplas.2022.103247
Received 11 November 2021; Received in revised form 16 January 2022;
Available online 1 February 2022

FCC- and $L1_2$-structured samples have identical crystal structures, but exhibit completely different mechanical properties (Liu, 2013; Yang et al., 2020). Therefore, the deformation behavior of $L1_2$-structured HEAs must be systematically investigated.

Grain boundaries (GBs) are known to strongly affect plastic deformation behavior (Di Gioacchino and Quinta da Fonseca, 2015; Lim et al., 2011; Wang et al., 2014). Similar microstructures include twin-boundary textures, second phases, and deformation substructures (Miao et al., 2009; Stinville et al., 2015). Because dislocations accumulate at GBs during plastic deformation, the local stress increases sharply and exceeds the critical resolved shear stress (CRSS) to activate dislocations in the adjacent grains (Bieler et al., 2019, 2014; Guo et al., 2014). This behavior balances the heterogeneous stress distribution and prevents crack initiation in the GBs. Moreover, deformation twins are considered an important alternative deformation mechanism for avoiding deformation incompatibility in metals with low stacking fault energy (SFE) (Reddy et al., 2019). Deformation has been recently confirmed to not only vary among grains but also significantly change within grains (Di Gioacchino and Quinta da Fonseca, 2015; Perrin et al., 2010). Therefore, characterization of strain partitioning during deformation can assist in understanding the deformation behavior and fracture mechanism of a material.

In crystal plasticity theories, deformation occurring in a crystal is considered to develop in two parts: deformation of each grain through dislocation slip and an additional deformation near GBs to ensure that the material remains continuous (Lee, 1969). The local plastic deformation at the microstructure scale can be investigated using the lattice rotation relative to the initial orientation, and the crystal orientations can be examined by electron backscatter diffraction (EBSD). Moreover, a local misorientation, which relies on the variation in crystal orientation within a grain, is used as the strain estimation characteristic. The rotation path of crystal orientation within a grain can reflect the characteristics of the activated slip system, based on which certain classic models have been developed to describe lattice rotation behavior and the formation of texture in polycrystalline metals during the tensile process, such as the Sachs, Taylor, self-consistent, grain interaction, and mathematical models (Chen et al., 2013; Hosford, 1977; Hutchinson, 1970; Mika and Dawson, 1998). The Sachs model was considered for analyzing slip systems in the present study; herein, the stress conditions in each grain are assumed to be equivalent to those corresponding to the activation of CRSS. Although EBSD can measure lattice rotation and misorientation distribution, it is limited in terms of characterizing strain distribution; therefore, digital image correlation (DIC) can assist in reliably measuring strain partitioning (Joo et al., 2013). Plastic deformation, in combination with the initial orientation figure, can be related to the microstructure, original crystal orientation, local Schmid factors, and Taylor factors. These analyses can be collectively used to assess the influences of microstructural features and deformation behavior.

FeCoNiV HEA has been reported to undergo the FCC–$L1_2$ phase transition below 780 °C, yielding the $L1_2$ phase at room temperature (Wang et al., 2019). In contrast to the FCC-structured sample, the $L1_2$-structured sample exhibits a higher strain-hardening rate, increased tensile strength, and considerable plasticity. Different deformation behavior and fracture mechanisms clearly exist in the FCC/$L1_2$-structured FeCoNiV HEAs. Therefore, the FeCoNiV HEA is suitable for a detailed study of the deformation behavior of the $L1_2$ structure. In the present study, the polycrystalline deformation associated with slip, material rotation, and spatial distributions of plastic strain was examined by in situ high-resolution DIC (HR-DIC) and EBSD methods to elucidate the deformation behavior and fracture mechanism in an $L1_2$-structured HEA.

2. Experimental section

2.1. Material and microtensile testing

An alloy ingot with a nominal composition of equiatomic FeCoNiV HEA was prepared by arc melting a mixture of pure metals (purity > 99.95%) under a Zr-gettered high-purity Ar atmosphere and subsequently drop-casting the product into a Cu mold with dimensions of $7 \times 10 \times 100$ mm^3. The samples were first hot-rolled at 1000 °C with a thickness reduction of 3 mm and subsequently homogenized at 1200 °C for 24 h prior to water quenching to eliminate casting defects and chemical inhomogeneities. A suitable equiaxed grain structure (grain size ~10 μm) was obtained by cold rolling (reduction ratio: 85%) and recrystallization at 1000 °C for 30 min, followed by immediate water quenching. The $L1_2$ structure was achieved by annealing at 755 °C for 12 h followed by water quenching. Differential scanning calorimetry (DSC) measurements were carried out to determine the phase transformation temperature on a 96 Line (SETARAM Instrumentation, France).

The original microstructure of the two studied alloys were analyzed using a combination of X-ray diffraction (XRD), EBSD, and transmission electron microscopy (TEM). The XRD (D8 ADVANCE Da Vinci, Bruker, Germany) analysis was performed on the FCC- and $L1_2$-structure samples for phase identification, with an incident beam of Cu Kα radiation (wavelength = 1.5418 Å). TEM investigations were performed using a JEM-2100F (JEOL, Japan) at an accelerating voltage of 200 kV. Microtensile tests were performed on plate-type specimens with a gage length of 4 mm and cross-section of 1×2 mm^2 using a universal testing machine at a quasistatic strain rate of 0.1 mm/min (MTEST 5000 W Tensile Stage, GATAN, United Kingdom). At each strain level, the tensile tests were interrupted and the stress state was maintained to acquire scanning electron microscopy (SEM)/EBSD-related information in situ for the specimens (LYRA3 GMU, TESCAN, Czech Republic).

2.2. Analysis of EBSD data

In situ EBSD analysis enables examination of active slip systems, lattice rotation, and textural evolution during deformation. The sample surface was polished to remove the surface stress layer, and the acquisition was performed using HKL Channel 5 software (UK). At each strain step (i), the resulting average Euler angles (φ_1, Φ, φ_2) were determined to describe the crystalline orientation. The rotation axis, $\boldsymbol{R}_a$, and the rotation angle, θ, between these steps were calculated from the Euler angles (see Appendix A). The rotation

path was determined as a characteristic of the activated slip system, with each slip system leading to a distinct rotation axis (Margulies et al., 2001; Winther, 2008). Therefore, the rotation of the slip-induced rotation axis between steps *i* and *j* for each slip system caused by actual changes in orientation could be computed, and the magnitude of the rotation of this axis for the operating slip system was expected to be the lowest (Hémery and Villechaise, 2019). However, this approach implies that only a single slip can be activation during deformation process, which is not consistent with the actual scenario involving the FCC-structured sample. An alternative effective approach involves calculating the theoretical rotation paths for all possible slip systems and comparing them with the actual rotation paths in an inverse pole figure (IPF) (Chen et al., 2013). The theoretical rotation paths were calculated using the Sachs model; essentially, the rotation axis was determined using Euler angles and the theoretical slip system, the crystal was rotated by a certain angle, and the direction of the loading axis in the new crystal coordinate system was determined (see Appendix B). [001]-[101]-[111]

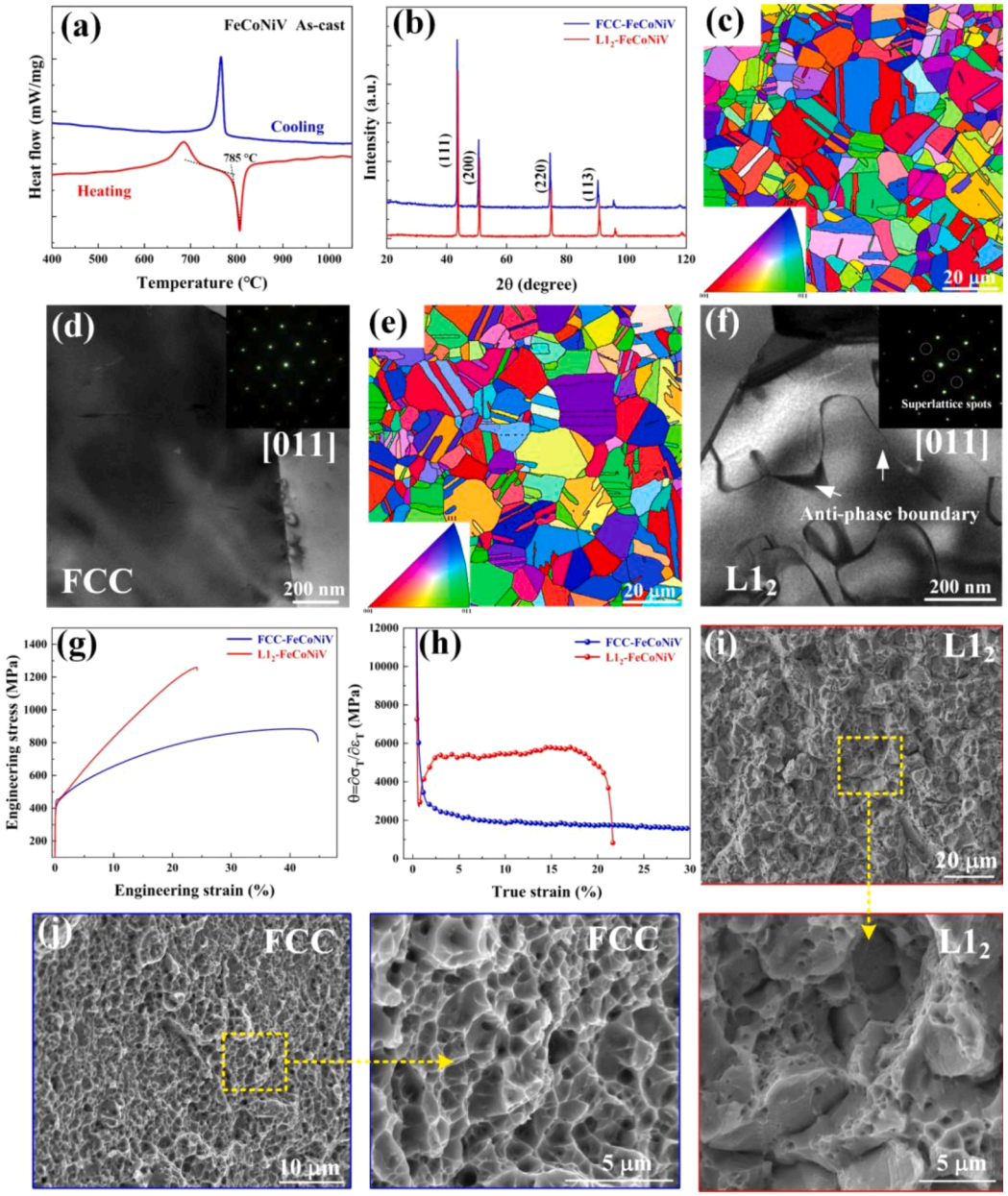

Fig. 1. (a) DSC heating and cooling curves of as-cast FeCoNiV high-entropy alloy (HEA) obtained at a constant rate of 10 °C/min from 50 to 1100 °C; (b) XRD patterns of the FeCoNiV alloy; (c) An EBSD inverse pole figure (IPF) and (d) a selected area electron diffraction (SAED) pattern with a bright-field (BF) image of FCC-structured FeCoNiV HEA; (e) An EBSD IPF and (f) an SAED pattern with a dark-field (DF) image corresponding to a superlattice spot (100) of L1$_2$-structured FeCoNiV HEA; (g) Engineering stress–strain curves of FeCoNiV HEA; (h) Work hardening rate–true strain curves of FeCoNiV HEA; (i, j) SEM images of the fracture surfaces of (i) L1$_2$- and (j) FCC-structured FeCoNiV HEAs.

IPF was used to display the results owing to cubic symmetry. During the calculation of each rotation path, only one active slip system was considered for the Sachs model, and four slip systems were considered for the rotation path based on the magnitude of their Schmid factors.

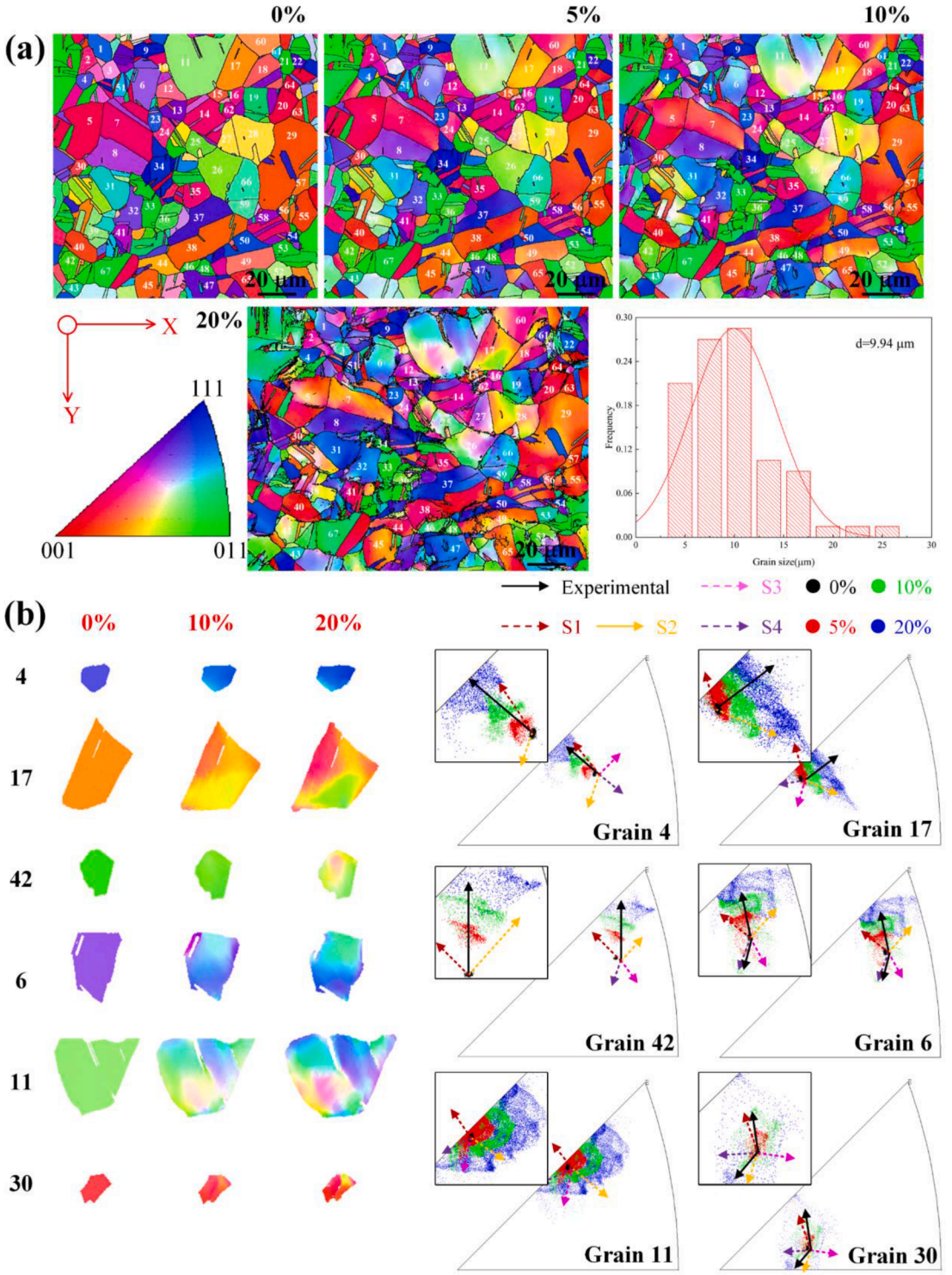

Fig. 2. (a) Grain orientation maps of the FCC-structured sample subjected to different levels of strain (0%, 5%, 10%, and 20%). (b) Evolution of grain orientation parallel to the loading direction of certain grains under tensile deformation in an IPF.

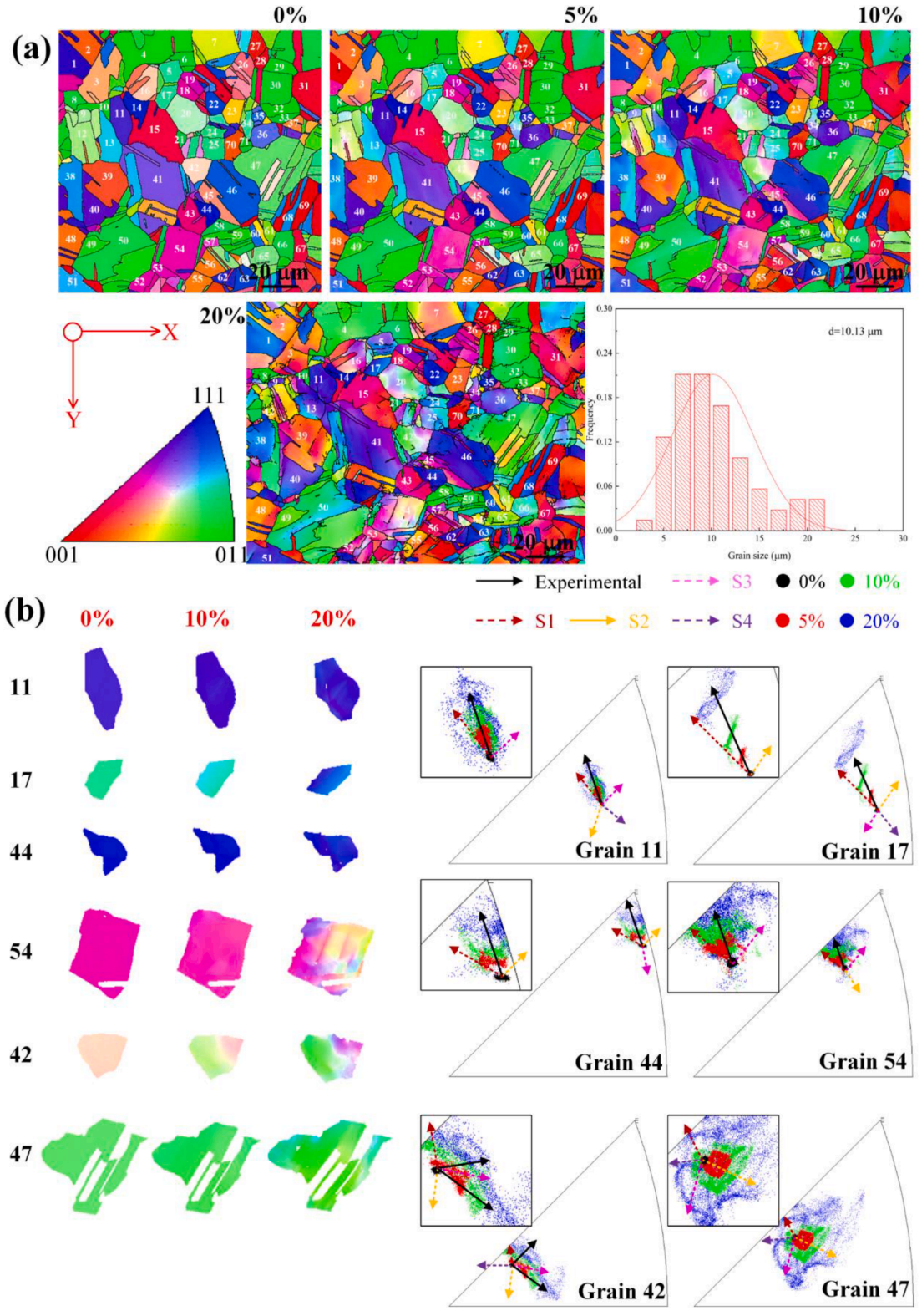

Fig. 3. (a) Grain orientation maps of the $L1_2$-structured sample subjected to different levels of strain (0%, 5%, 10%, and 20%). (b) Evolution of grain orientation parallel to the loading direction of certain grains under tensile deformation in an IPF.

Moreover, the samples used for HR-DIC analysis were examined by EBSD to define GBs, twin boundaries, and Euler angles; to plot {111} plane traces; and to calculate the Schmid factors of individual grains in each slip system prior to the tensile tests.

2.3. HR-DIC measurements

Prior to conducting the tensile tests for HR-DIC analysis, the sample surface was marked with a nanoscale speckle pattern after the

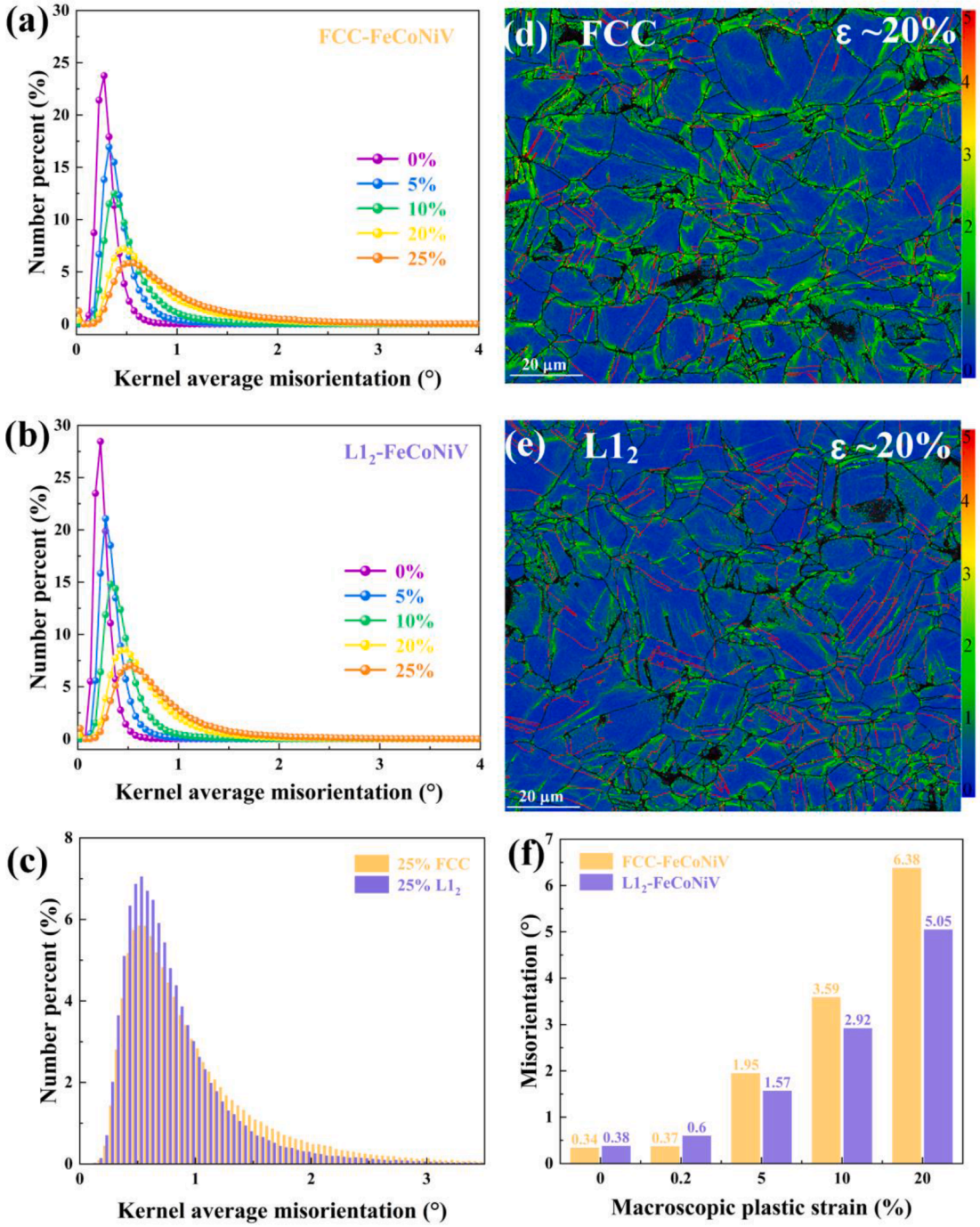

Fig. 4. (a–c) Distributions of the kernel average misorientation (KAM) values at different strain levels (0%, 5%, 10%, 20%, and 25%) in the FCC/$L1_2$-structured samples. (d, e) KAM values of the FCC/$L1_2$-structured samples subjected to a strain of 20%. (f) Variation in the average grain misorientation with macroscopic plastic strain in the FCC/$L1_2$-structured samples.

EBSD analysis. Sufficiently fine speckles on the surface of the tested specimens were required to enhance the spatial resolution of DIC for relating the deformation to the microstructure. The deposition of nanometer-sized copper, colloidal silica, and gold particles has been recently used to resolve strain localization at the microstructure scale in various structural materials (Lim et al., 2014; McMurtrey et al., 2014; Tasan et al., 2014). In the present study, gold speckles were homogeneously distributed. Image acquisition was performed at a resolution of 4096 × 3072 pixels and at a magnification of 9000 × , which corresponds to a field of view of 30.8 × 23.1 μm. DIC analysis in the deformation sequence was performed using Vic-2D commercial software (Correlated Solutions, USA). The displacement field, **u**(X), provided by the DIC analysis was used to calculate the effective maximum shear strain, γ_{max}, and material rotation, ω_3. Moreover, γ_{max} and ω_3 assisted in representing the distribution of the plastic strain and material rotation in an area of interest.

3. Results

3.1. Structural and tensile characteristics

Fig. 1(a) shows continuous DSC heating and cooling curves of the as-cast FeCoNiV HEA obtained at a constant rate of 10 °C/min from 50 to 1100 °C. An endothermic peak corresponding to the disordering transition and an exothermic peak corresponding to the ordering transition were obtained in the heating and cooling curves, respectively. The endothermic reaction in the heating process was initiated at 785 °C, and the exothermic reaction in the cooling process commenced at 776 °C. In the XRD patterns of the FeCoNiV alloy (Fig. 1(b)), only one set of characteristic peaks of the FCC structure could be clearly identified in both samples. However, the lattice parameter decreased from 3.5892 to 3.5758 Å after annealing. The FCC structure was confirmed by EBSD IPFs, a representative TEM micrograph, and the corresponding selected area electron diffraction (SAED) pattern, as shown in Fig. 1(c, d). The EBSD IPFs, SAED pattern, and dark-field figure corresponding to the superlattice spot (100) (Fig. 1(e, f)) showed a typical ordered domain and anti-phase domain boundaries of the $L1_2$ phase. The engineering stress–strain curves, work-hardening-rate curves, and fracture surfaces of the $L1_2$- and FCC-structured FeCoNiV alloys at ambient temperature are shown in Fig. 1(g–j), respectively. The tensile and work-hardening-rate curves showed clear differences in the deformation behavior between the $L1_2$- and FCC-structured samples. Moreover, the fracture surface of the FCC-structured sample was primarily composed of small dimples, whereas the $L1_2$-structured sample displayed mixed fracture features of the dimples and intergranular fracture. Theoretically, the $L1_2$ phase has an identical crystal structure to that of the FCC phase; the different mechanical properties of these samples are noteworthy in this regard. Although research on the deformation and fracture mechanisms of the FCC phase is relatively mature, those of the $L1_2$ phase, especially in HEAs, are not sufficiently clear. Therefore, in situ EBSD was combined with an in situ HR-DIC method to elucidate the deformation behavior and fracture mechanism in an $L1_2$-structured HEA.

3.2. In situ EBSD analysis

3.2.1. Microstructural evolution during tensile deformation

The microstructural evolution of FCC- and $L1_2$-structured FeCoNiV alloys during deformation was investigated. Fig. 2(a) shows the grain orientation maps of the FCC-structured sample obtained in situ at strain levels of 0%, 5%, 10%, and 20%. The direction normal to the plate samples represents the view direction, and the horizontal direction (X) represents the loading direction. Because annealing twin boundaries influence deformation, they were regarded as different grains. Pixels with a misorientation angle smaller than 10° with respect to the neighboring pixels were considered to constitute one grain in the undeformed sample, and the grains in the deformed samples were assessed in accordance with the undeformed samples. Consequently, 67 grains (denoted 1–67) were clearly identified in the IPFs obtained at different strains. Each grain had a uniform orientation prior to the plastic deformation. With an increase in strain, the orientation of each grain changed to varying degrees, and different orientations appeared within the grain upon tension to a strain of 5%, that is, in grains 6, 11, 17, and 26, implying inhomogeneous deformation within them. Multiple subregions with different orientations appeared within individual grains at a strain of 20%. Moreover, significant misorientations were observed near certain annealing twin boundaries and GBs. Fig. 3(a) shows the grain orientation maps of the $L1_2$-structured sample obtained at four different tensile strain levels. Seventy-one grains, including annealing twins, were selected for tracking analysis. The similar results of the $L1_2$-structured sample to those in Fig. 2(a) indicate that the grain orientation significantly varied with increasing deformation, with notable misorientation occurring within certain grains that eventually evolved into a substructure. However, the number and degree of substructures in the $L1_2$-structured sample macroscopically appeared to be lower than those in the FCC-structured specimen.

The differences in the microstructural evolution of the FCC- and $L1_2$-structured samples undergoing tensile deformation were analyzed using kernel average misorientation (KAM) to evaluate the local strain distributions. As shown in Fig. 4(a), a larger plastic deformation led to greater deformation-induced inhomogeneity within each grain in the FCC-structured sample. Similarly, the KAM values tended to increase in the $L1_2$-structured sample with gradually increasing strain (Fig. 4(b)). Compared with the KAM data of the FCC sample obtained at a strain of 25%, the proportion of KAM > 1° in the $L1_2$ sample was smaller than that of the FCC sample, indicating a smaller deformation inhomogeneity in the $L1_2$ sample (Fig. 4(c)). The KAM distribution maps acquired at a strain of 20% (Fig. 4(d, e)) indicate that the local strain was larger at the grain, twin, and substructure boundaries. Interestingly, a wider region near the GBs in the FCC sample had a large KAM value (>1°), whereas only a narrow region near the GBs had a large local strain in the $L1_2$ sample. In addition, the misorientation within an individual grain was used to reflect the degree of substructural deformation. The misorientations within the aforementioned ~70 grains at several tensile strain levels were quantified (Fig. 4(f)). The results suggest that during the early deformation period (<0.2%), the average misorientation within grains in the two samples was not significantly

different; however, the misorientation within grains in the FCC sample significantly increased compared to that of the $L1_2$ sample with increasing strain, indicating greater deformation-induced inhomogeneity and a more intricate substructure in the FCC-structured sample.

3.2.2. Prediction of slip activity and deformation structure

Active slip systems are investigated because, typically, the deformation structure depends significantly on them. The rotation path is a characteristic of active slip systems, and the lattice rotation path can be manifested by the evolution of the grain orientation parallel to the loading direction (Hémery and Villechaise, 2019; Margulies et al., 2001). Fig. 2(b) shows the variation in orientation and shape of certain grains with increasing strain, along with the tensile-axis-based evolution of the selected grains in IPFs. The lattice rotation was observed to occur continuously in the grains during the deformation (following the sequence of black, red, green, and blue dots); the experimentally observed rotation paths are indicated by the solid black vectors. The tensile axes of all the differently oriented grain rotation paths deviated from the <112> orientation, which is the stable end position under the single slip condition. Moreover, significant misorientations were observed within almost all grains after large deformations, as shown by the considerable difference in color within the grains and the splash pattern in the IPFs. The grains could be classified into two types based on the aforementioned orientation evolution; these were quantitatively defined by the number of rotation paths in the present study. Type I grains included those with one primary rotation path despite a large misorientation within the grain at large deformations and a splash pattern in the IPFs, that is, G4, G17, and G42; type II grains included those with two or more rotation paths that indicate the presence of a deformation substructure, that is, G6, G11, and G30. Twenty-five grains of the selected 67 grains belonged to type II, and the remaining 42 grains belonged to type I in the FCC-structured sample. Fig. 3(b) shows that the two types of grains were also observed in the $L1_2$-structured sample (type I: G11, G17, and G44; type II: G54, G42, and G47). The statistics of the acquired data indicate that only 16 grains of the observed 71 grains belonged to type II. In addition, the misorientations of these two types of grains were counted, and misorientation within grains plotted against the grain size of individual grains at a strain of 20% for the FCC- and $L1_2$-structured samples, respectively, as shown in Fig. 5(a, b). The classification of grain type has little relation with grain size. Most type I grains had an extremely low misorientation (<5°), whereas most type II grains had a misorientation of greater than 5°. Moreover, the misorientation within grains was clearly affected by other factors such as grain orientation and the surrounding environment of grains. Therefore, based on the previous results, the lower misorientation in $L1_2$-FeCoNiV was presumably due to the fewer type II grains and the smaller local strain in them.

Experimentally verified that the rotation path predicted by the Sachs model in a polycrystalline aluminum alloy was consistent with the experimentally measured paths with minor deviations (Chen et al., 2013). Al alloys,FCC-HEA, and $L1_2$-HEA have identical crystal structures, close-packed planes, and close-packed directions. Therefore, the Sachs model was considered a suitable method for analyzing slip systems in the present study and to theoretically predict the rotation paths induced by the slip system for each grain. The Schmid factors of all slip systems were computed for each grain, and the slip system was sequentially numbered based on the magnitude of the Schmid factor, that is, S1, S2, S3, and S4. The carmine, faint yellow, magenta, and purple dotted arrows in Fig. 2(b) and Fig. 3(b) represent the theoretical grain rotation paths generated by the activation of a single slip system; it is worth noting that the lengths of the lines are arbitrary and do not represent the magnitude of the rotation angle. The results indicate that the {111}<110> slip system was activated in both the FCC- and $L1_2$-structured samples, and at least two main slip systems were activated in almost all the grains according to the prediction. The slip systems with maximum and secondary Schmid factors were often activated first. Moreover, slip systems with smaller Schmid factors (approximately 0.3) were activated in certain grains, especially in type II grains. Among them, the main rotation paths in the type I grains were generated by the activation of two sets of slip systems; therefore, the IPF

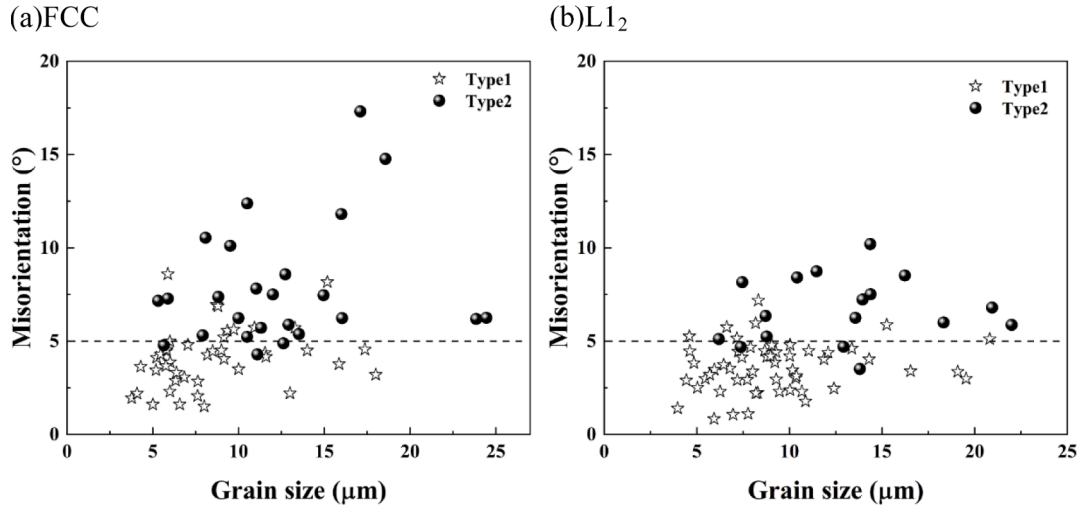

Fig. 5. Misorientation within grains plotted against the grain size of individual grains at a strain of 20% for the (a) FCC- and (b) $L1_2$-structured samples.

showed a clear radiative feature. More than three slip systems were activated in the type II grains, and each major slip rotation path was generated by more than two activated slip systems, which reflected the formation of deformation substructures. According to the statistics, the number of deformation substructures in the $L1_2$ sample was less than that in the FCC sample, which explains the lower average misorientation within the grains of the $L1_2$ sample.

3.2.3. *Lattice rotation in grains*

The lattice rotation rate is considered an important factor for describing the formation of the deformation texture. A linear relationship between the lattice rotation and macroscopic plastic strain has been reported, and the predicted lattice rotation rate is directly proportional to the plastic shear rate (Guan et al., 2017). The lattice rotation relative to the initial orientation at each step was calculated using Eq. (A3). Scheriau investigated the evolution of orientation-related changes in polycrystalline copper, nickel, and iron during tensile tests and highlighted the significant influence of grain size on the changes in orientation during plastic deformation (Scheriau and Pippan, 2008). Therefore, the angle of rotation at a strain of 20% was plotted against the grain size for both FCC- and $L1_2$-structured samples to investigate the influence of grain size on the rotation angle (Fig. 6). No clear relationships between the grain size and the rotation angle could be derived through this investigation. Additionally, the influence of the Schmid factor on the magnitude of the rotation was probed, and the maximum Schmid factor of the slip system for each grain was also plotted against the angle of rotation at a strain of 20%. Grains with high values of the maximum Schmid factor exhibited both high and low angles of rotation. Therefore, the grain size and maximum Schmid factor had no clear influence on the magnitude of rotation in both the FCC- and $L1_2$-structured samples. This is because the local plastic deformation and rotation of each grain depend on the grain orientation, the activated slip system, and the influence of surrounding grains such that the plastic deformation and rotation angles of each grain were not the same under similar macroscopic deformations (Tang et al., 2020). To quantitatively assess the average lattice rotation behavior, the angle of rotation was averaged over the approximately 70 grains and plotted against the macroscopic plastic strain (Fig. 7). The average angle of rotation was found to increase linearly with the macroscopic plastic strain via a linear regression. An offset of approximately 0.3° was observed toward the end of the elastic regime, which is related to rigid body rotation, and the obtained regression coefficient of approximately 0.998 indicates that the statistics were meaningful. However, as shown in Fig. 7, a significant deviation from linear regression occurred in the $L1_2$-structured sample at a strain of 0.2%. The possibility of rigid rotation of the specimens was eliminated by calculating the rotational axis for each grain in the coordinate system of the specimen. Therefore, the

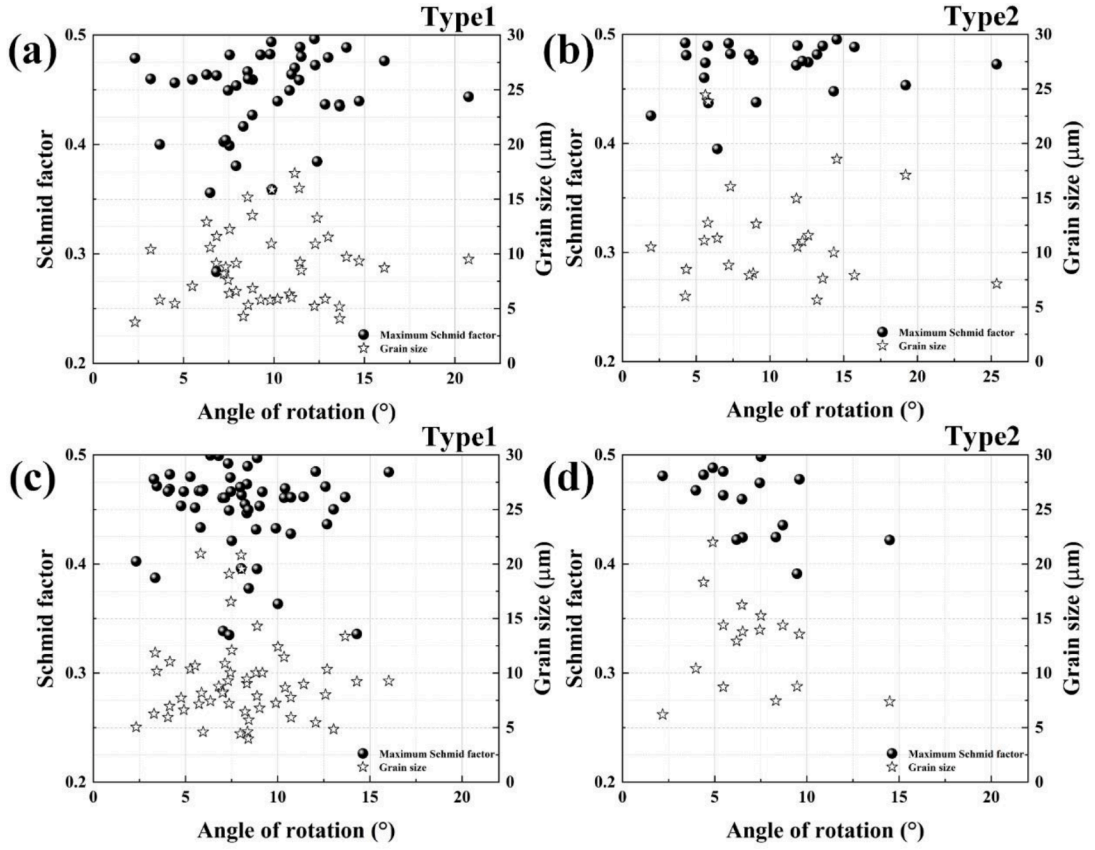

Fig. 6. Schmid factor and grain size plotted against the average angle of rotation of an individual grain at a strain of 20% for (a, c) type I and (b, d) type II grains in the FCC- (a, b) and $L1_2$-structured (c, d) samples.

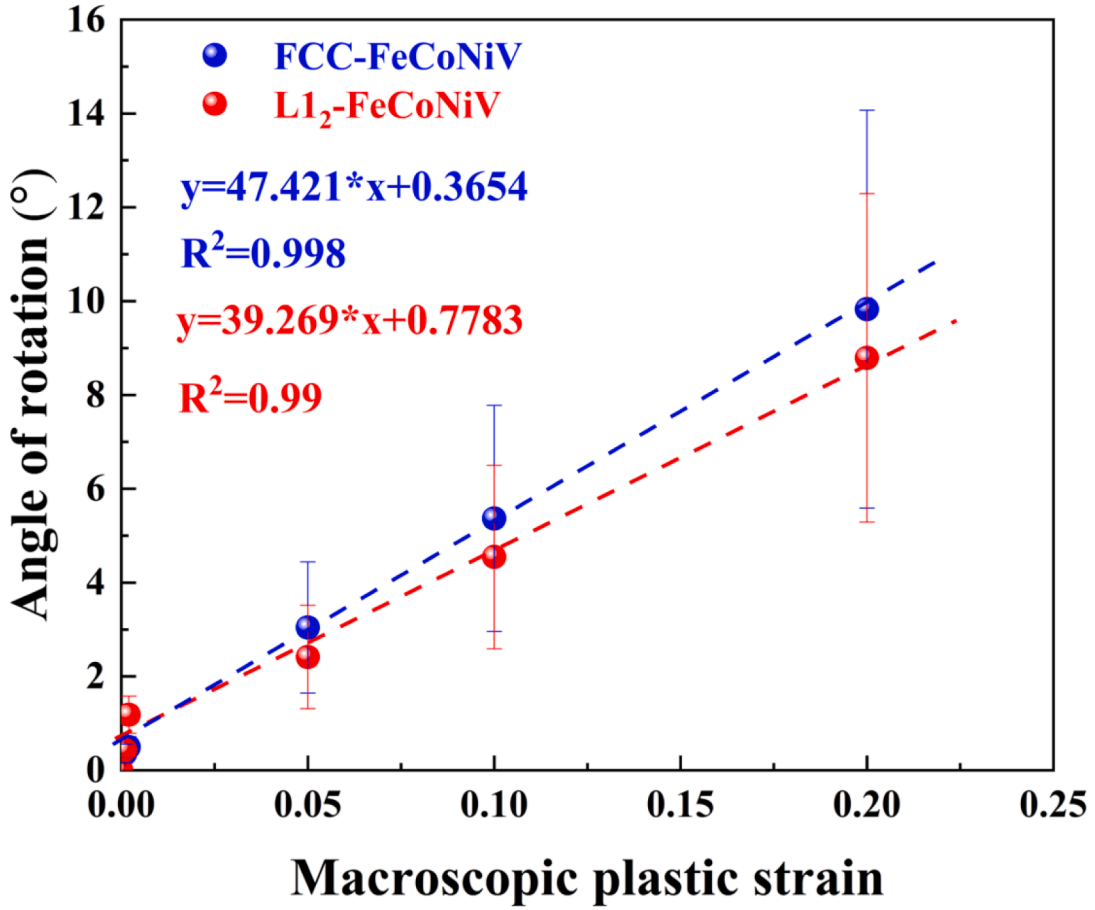

Fig. 7. Linear dependence of the average angle of rotation over nearly 70 grains on the macroscopic plastic strain.

dislocation slip behavior significantly changed during the deformation of the $L1_2$-structured sample. Moreover, slopes of 47° and 39° were obtained for the FCC- and $L1_2$-structured samples, respectively. The significant difference highlights the strong dependence of the operating slip behavior on the lattice rotation behavior of the two samples.

3.3. HR-DIC analysis

3.3.1. Trace analysis for slip activity

Compared with rotation path analysis, slip trace analysis can provide more accurate information for ensuring an active slip system for individual grains. In particular, the traces of different slip planes can be clearly distinguished for the FCC structure with only four slip planes and high symmetry. Prior to the tensile tests, EBSD measurements were performed to identify the GBs and orientation of individual grains, as shown in Fig. 8(a) and Fig. 9(a). SEM images of the undeformed samples are shown in Fig. 8(b) and Fig. 9(b), and the process of preparing speckles on the sample surface resulted in certain changes in the grain morphology. Certain grains in the FCC sample (B1–B10, B15) were selected for slip activity analysis at a strain of 18% (Fig. 8(c)). A clear slip trace in multiple directions was observed in each grain in the SEM image, and the visible slip traces were parallel to the identified {111} plane (indicated by dark yellow lines), implying the activation of at least two types of {111}<110> dislocations in each grain. Moreover, traces in different regions within the grain indicate that different types of dislocations were initiated in different regions, and the slightly curved traces suggest the presence of interactions between the different types of dislocations. These direct observations from the trace analysis method are consistent with the results from the rotation-path-predicting slip activity method in the aforementioned in situ EBSD analysis.

Similarly, the {111} plane traces on the surface were calculated based on the crystal orientation of individual grains in the $L1_2$ sample (Fig. 9(c)). In contrast to the FCC sample, clear slip traces were not observed on the $L1_2$ sample surface subjected to a similar degree of deformation, implying that the dislocations were severely hindered; therefore, slip bands were not clearly visible on the surface. Slip traces in multiple directions could be observed in only a few grains, in contrast to the results predicted by the in situ EBSD data. Considering that the slip band structure could be destroyed by the dislocation behavior in the $L1_2$ sample, the slip traces were not sufficient to accurately describe the slip activity; therefore, combining this analysis with the in situ EBSD method can be effective in

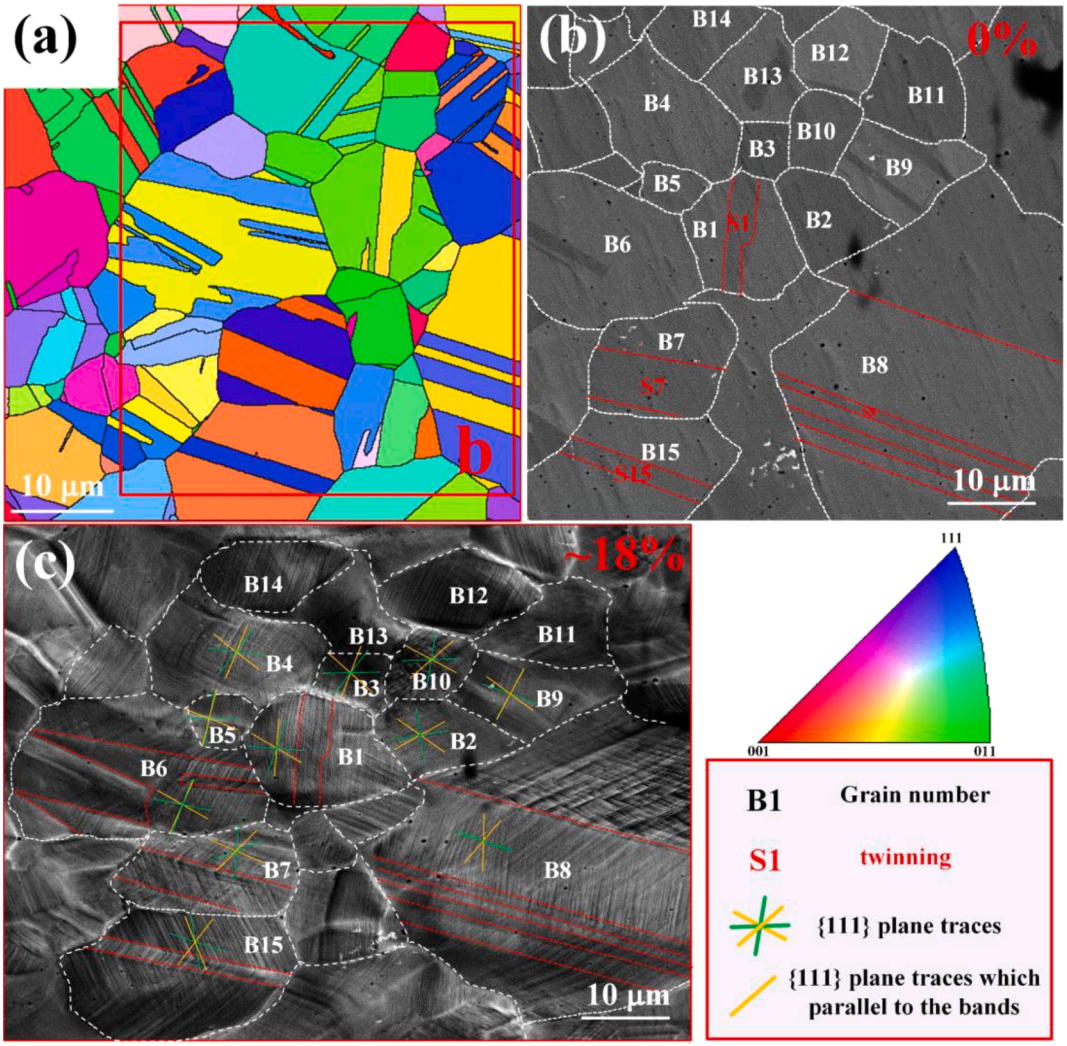

Fig. 8. (a) IPF maps of the FCC-structured sample at a tensile strain of 0%; SEM images corresponding to the highlighted region in (a) at strains of (b) 0% and (c) 18%.

analyzing slip activity in this context.

3.3.2. Plastic strain and material rotation

In situ observation of the strain distribution during deformation can assist in monitoring the deformation behavior of materials. Maps of γ_{max} of the FCC sample obtained in a region of interest at macroscopic strains of 2%, 4%, 11%, 16%, and 18% are shown in Fig. 10(a–e), respectively. Evidently, the distribution of the shear strain was heterogeneous from the early stage of deformation. The shear strain was primarily concentrated between the shear bands, which corresponded to the slip traces in the SEM images. As deformation progressed, the grains with a higher Schmid factor deformed first and activated a slip system according to the magnitude of the Schmid factors (i.e., B1, B3, and B4) (Fig. 10(a)). An additional slip system with a large Schmid factor in a few grains was activated with grain rotation, as shown in S1. Furthermore, most of the grains were activated by more than two sets of slip systems to coordinate deformation, as shown in Fig. 10(c). Among them, certain activated slip systems had a small Schmid factor of approximately 0.35, indicating that the local stress caused by inhomogeneous deformation exceeded the CRSS for activating the slip system. At a macroscopic strain of 16%, the strain distribution map showed significant strain accumulation at the GBs, with the magnitude exceeding that between slip bands within the grains. As shown in Fig. 10(e), typical behavior was observed at the GBs between B1 and B6 and between B1 and B4, with the dislocation spreading at a certain depth from the GB to the interior, forming a substructure region at a certain range. The formation of a visible substructure within the grain can be attributed to the local stress accumulated at the GBs, leading to the activation of a compatible slip system, which helped alleviate the incompatibilities at the GBs.

Additionally, maps of γ_{max} of the $L1_2$ sample were obtained in a region of interest at macroscopic strains of 2%, 4%, 11%, 16%, and 18% (Fig. 11(a–e)). In contrast to the FCC sample, the distribution of shear strain was relatively uniform within the grain. The slip

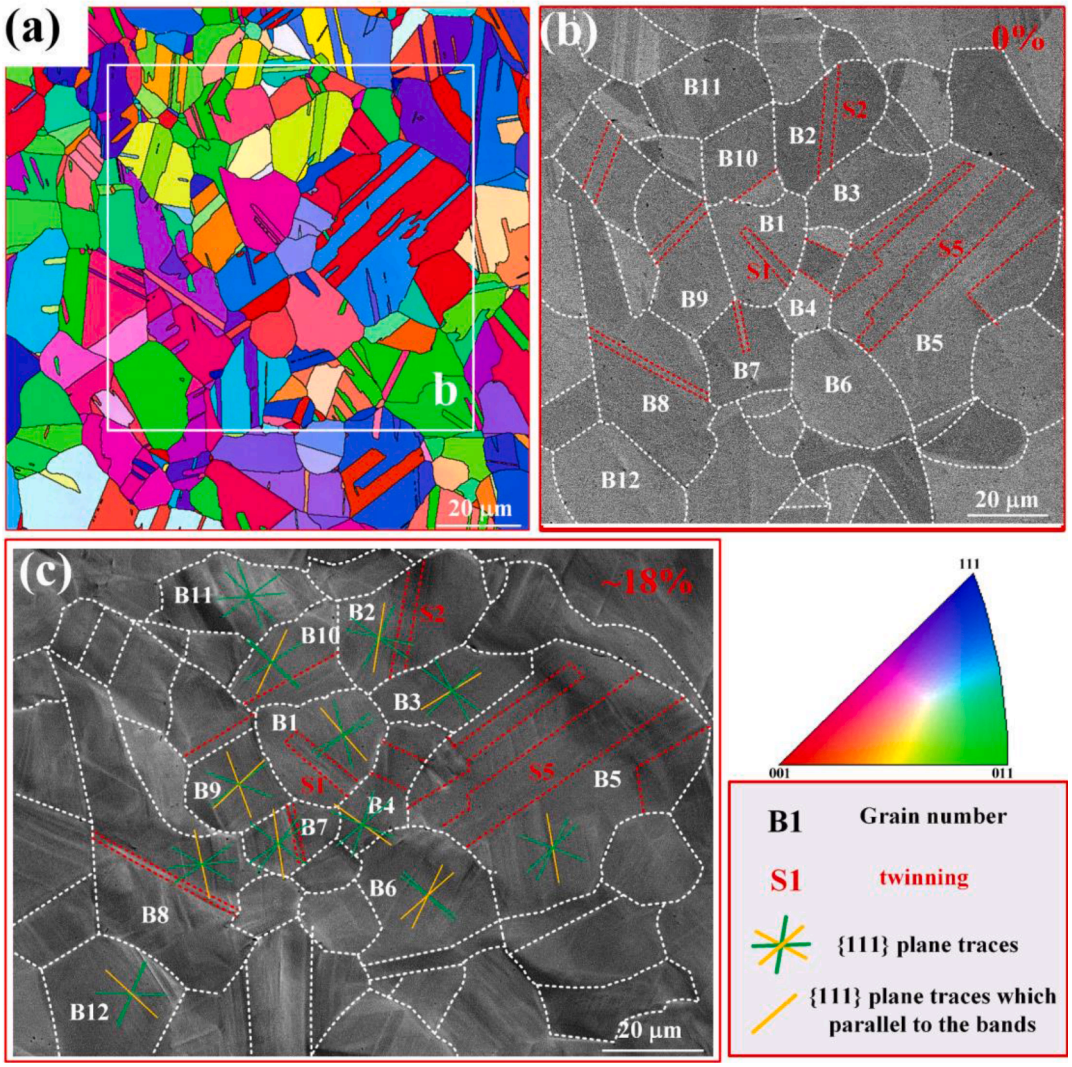

Fig. 9. (a) IPF maps of the $L1_2$-structured sample at a tensile strain of 0%; SEM images corresponding to the highlighted region in (a) at strains of (b) 0% and (c) 18% strain.

system with the maximum Schmid factor was activated first during the initial plastic deformation, and the second set of slip systems was activated as the deformation continued (B5 and B6). In Fig. 11(d, e), the regions in which two sets of slip systems were concurrently activated became the maximum local shear strain regions, indicating that the strain continued to exist in the regions of aggregated dislocations. At this stage, strong local stresses accumulated on the GBs in both the FCC and $L1_2$-FeCoNiV HEAs owing to considerable deformation within the grains. In the FCC-FeCoNiV HEA, the active compatible slip system was the key deformation form that released the local stress and alleviated the incompatibilities at the GBs. In the $L1_2$-FeCoNiV HEA, the low γ_{max} at the GBs at this stage indicates that the accumulated stress at the GBs could not be released in this manner. The creation of a compatible slip system near GBs was resisted to a considerable degree in the $L1_2$ sample.

The EBSD results indicated that the lattice rotation caused by inhomogeneous deformation near the GBs in the FCC sample was larger than that in the $L1_2$ sample. According to A9 in Appendix C, in contexts where material rotation is associated with shear strain (unless pure shear occurs, for which $F_{12} \neq F_{21}$), the shear generally induces material rotation (Fig. 12). In domains where the bands had a positive slope, φ was negative in the bands of the 7%-strained sample; moreover, the material rotation near GBs intensified with increasing strain and had a positive or negative value (B1 and B4) in the FCC sample. After being subjected to similar macroscopic strains, the strain near GBs in the $L1_2$ sample was clearly lower than that in the FCC sample, which corroborates the fact that the stress accumulated near the portion of the GBs could not be released into the grain in the $L1_2$ sample.

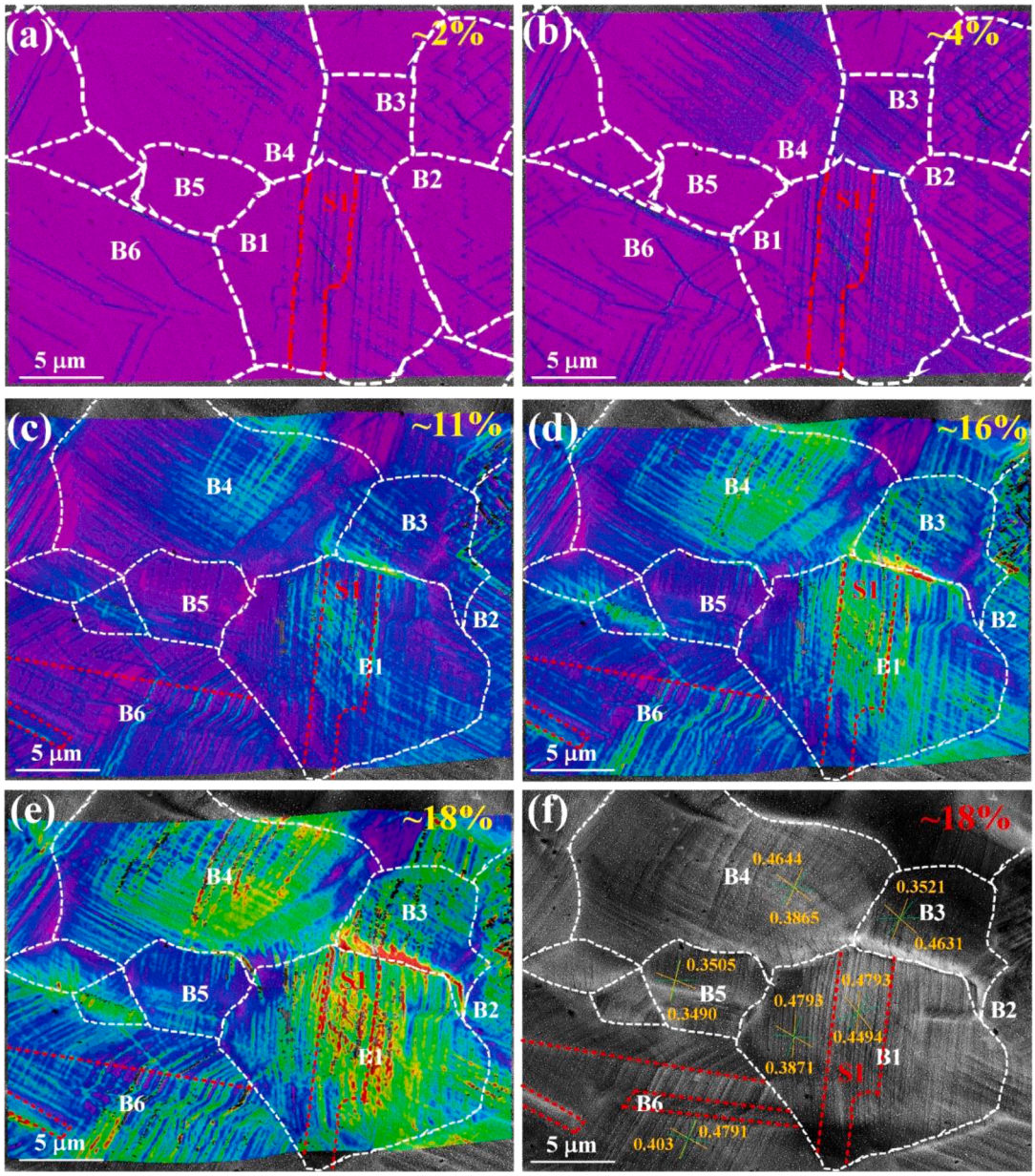

Fig. 10. (a–e) Maximum shear strain maps of the FCC-structured sample subjected to strains of 2%, 4%, 11%, 16%, and 18%, respectively. (f) SEM image of the 18%-strained FCC-structured sample that shows slip traces and Schmid factors.

4. Discussion

4.1. Slip system activation and hardening

The plastic deformation was remarkably heterogeneous from the start of the tensile deformation, and occurred as shear bands of regular spacing separated by regions with low strain. The measured slip bands were invariably well aligned with a highly stressed {111} slip plane trace. The observed distribution of strains resembles the typical deformation structures in deformed low-SFE materials; this is due to the low SFE of the examined alloy, which leads to a difficult cross slip, consequently promoting planar slip. At the start of the deformation, the primary and secondary slip systems were activated, and several non-co-planar slip systems were activated by the local accumulated stress with increasing strain. The aforementioned analysis indicates that lattice rotation within each grain was complex and heterogeneous, involving different rotation paths due to the activation of various slip systems in different domains within the grains. This deformation-based heterogeneity leads to the formation of a substructure and scattering of the orientation distribution.

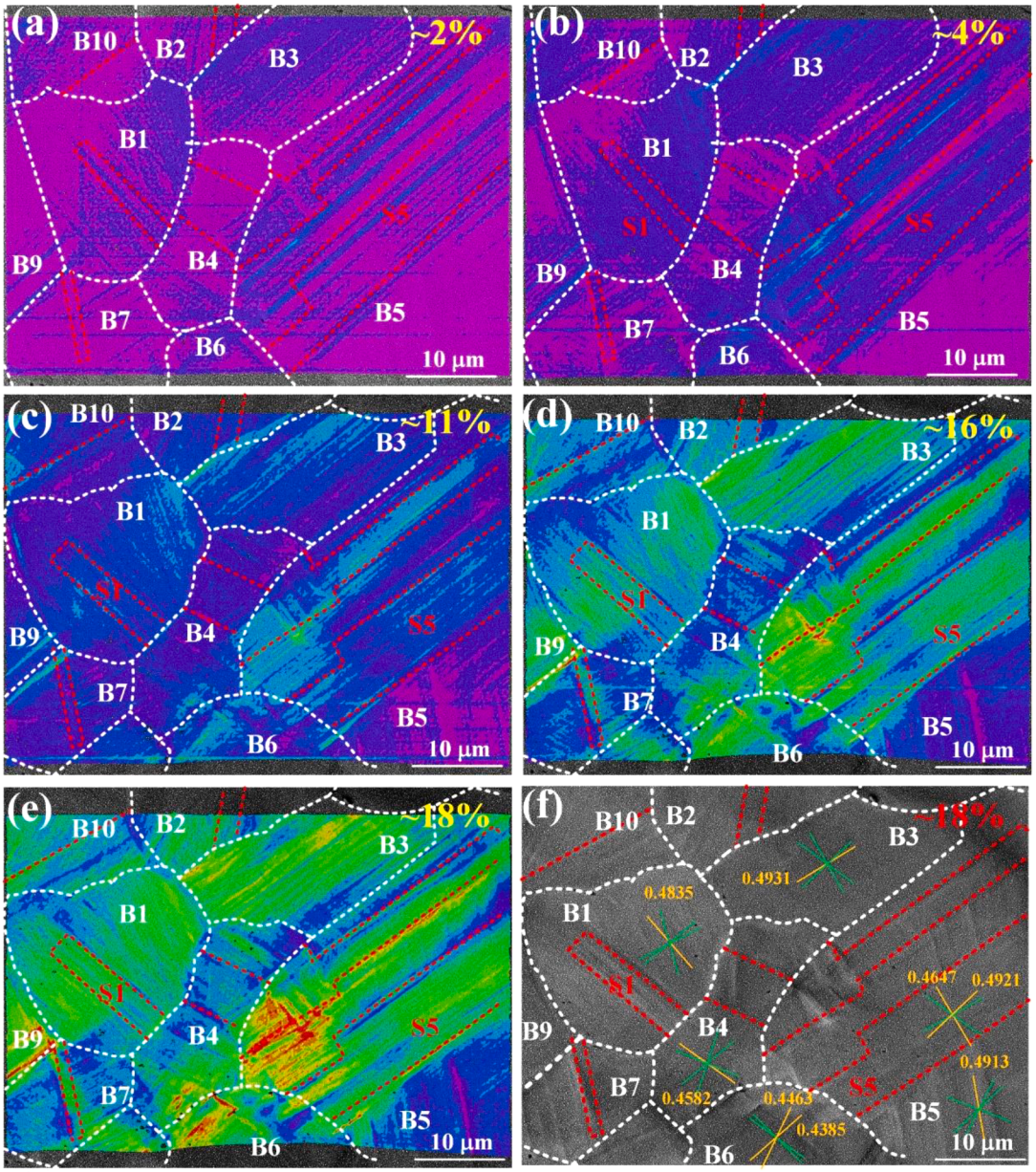

Fig. 11. (a–e) Maximum shear strain maps of the $L1_2$-structured sample subjected to strains of 2%, 4%, 11%, 16%, and 18%, respectively. (f) SEM image of the 18%-strained $L1_2$-structured sample that shows slip traces and Schmid factors.

Generally, the lattice rotation rate has a straightforward relationship in terms of the rate of dislocation slip in the slip system and the slip direction, which is controlled by the density of gliding dislocations and the frequency of jumps to overcome obstacles (Guan et al., 2017). Superdislocation pairs generate gliding dislocations at a higher density, whereas the barriers that must be overcome are similar, which leads to a higher lattice rotation rate in the $L1_2$ sample at the beginning of the deformation. As the deformation continued, the lattice rotation rate decreased to lower than that in the FCC sample, although the dislocation density was higher than that in the FCC sample, which indicated that the additional barriers to be overcome by the slip decreased the shear rate of the slip system. In addition, the rotation rate of the grains at the early stage of deformation in the $L1_2$ sample was higher than that in the later stage, confirming that the additional obstacle was not caused by the slip, but by the activation of multiple slip systems. The substantial barriers in ordered structures have been previously attributed to special configurations of superdislocations, including cross-slip-induced special jogs and the intersection of superdislocation-induced special jogs (Kear, 1964; 1966; Liu and Stiegler, 1984). The results show that the obstruction occurred after activation of the forest dislocation, especially in the process of GB emission dislocation into the grain. Therefore, the obtained results appear to corroborate the relationship between the hardening mechanism and the intersection of superdislocation-induced special jogs in the present study.

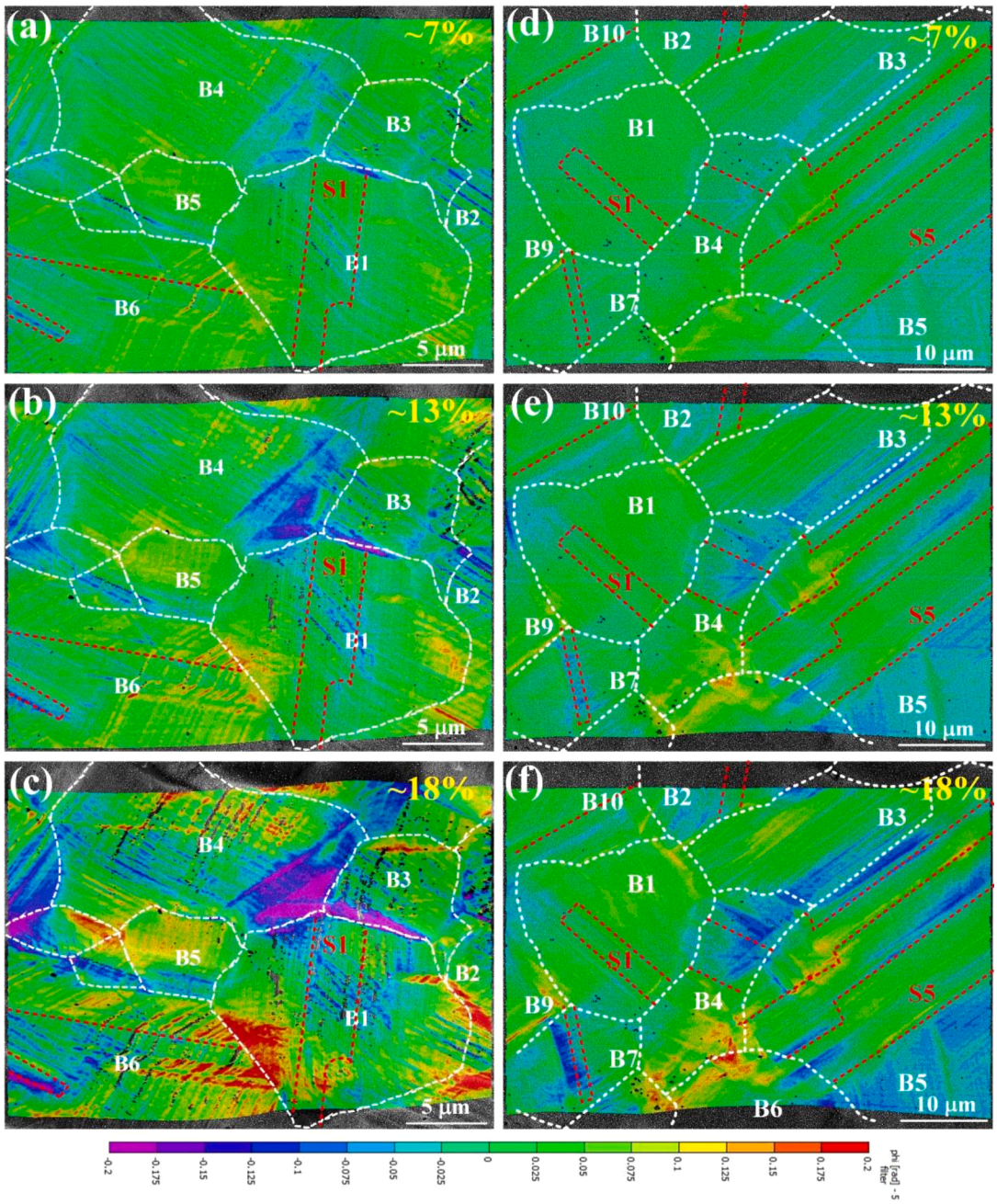

Fig. 12. DIC maps of the material rotation in the (a–c) FCC- and (d–f) $L1_2$-structured samples subjected to different strain levels (7%, 13%, and 18%).

4.2. Deformation incompatibility and fracture mechanism

The essential deformation behavior within grains was previously discussed. However, the development of the deformation structure is known to be a non-local effect that is influenced by neighboring grains. In particular, the intergranular deformation behavior of materials with fewer slip systems, such as magnesium alloys, significantly affects the mechanical properties. In these scenarios, there is limited incompatibility at GBs, which requires that adjacent grains have a suitable orientation, as described by the geometric compatibility factor (Bieler et al., 2014). For an FCC metal, each grain contains at least four slip systems with a high Schmid factor owing to the high symmetry. This reduces the incompatibility at the GBs; if incompatibilities arise, they can be accommodated by the activation of a complementary slip system (B1 and B4 in Fig. 10(e)). This complementary slip system is driven by accumulated stress at the GBs with constraints on both the range and magnitude, which corresponds to the formation of substructures within the

grains. Therefore, the formation of the deformation substructure can coordinate the intergranular deformation and ensure the stability of GBs. In contrast to the fracture morphology of the FCC-FeCoNiV HEA, that of the $L1_2$-FeCoNiV HEA clearly contained several intergranular fracture characteristics. Typical cracks occurring at the GBs were observed in the $L1_2$-FeCoNiV HEA sample with a macroscopic plastic strain of 18% (Fig. 13), in which no significant formation of a complementary deformation substructure was visible within the grains. Compared with the FCC-FeCoNiV sample, crack initiation at the GBs is possibly related to the deformation substructure. The EBSD and DIC results collectively demonstrate that the stress accumulated at the GBs was not sufficient to induce the formation of deformation substructures and could not be released via activation of compatible slip systems, which eventually led to crack initiation at the GBs.

Dislocation pile-up at a GB produces a net offset (equivalent to a microcrack) across atomic planes, which is a common dislocation mechanism for crack formation. Microcracks formed in this manner can continue to grow if the stress is sufficient, which can be described by the following equation (Voyiadjis and Yaghoobi, 2019):

$$K_I = \sigma\sqrt{\pi a} \geq K_{Ic}, \tag{1}$$

where the K_I is the stress intensity factor under plane strain with the first type of crack, K_{Ic} is the critical value of the stress intensity factor, σ is the stress, and a is the crack size. Moreover, the internal stress generated by the dislocation of the GB can activate dislocation of a neighboring grain, leading to the release of the pile-up dislocation at the crystal boundary.

$$\tau \geq \tau_0 + 2\tau^* r^{1/2} d^{-1/2}, \tag{2}$$

where τ is the internal stress, τ_0 is the shear stress that initiates slip when GBs offer no resistance, τ^* is the CRSS, r is the distance between the dislocation source and the GB, and d is the grain size. Generally, the stress is released via activation of the dislocation of the adjacent grains prior to the increase in the stress at the GB to the critical value of the crack instability. However, the activation of dislocation sources of neighboring grains in the $L1_2$-FeCoNiV crystals is subjected to additional resistance ($\Delta\tau_{extra}$) caused by special dislocation pinning mechanisms in the ordered structure. Therefore, when $\frac{K_{Ic}}{\sqrt{\pi a}} < M(\tau_0 + 2\tau^* r^{1/2} d^{-1/2} + \Delta\tau_{extra})$, microcracks formed at the GBs can continue to grow. As the constraints disappear, the accumulated internal stress at the GBs is gradually consumed until $K_I \leq K_{Ic}$, and the crack is temporarily stabilized. This provides a good explanation for the ductile rupture of the material as the primary form of failure.

Based on the observed deformation of the FCC/$L1_2$-FeCoNiV samples, their deformation behavior and fracture mechanisms are illustrated in Fig. 14. As the deformation is initiated, the primary and secondary slip systems are activated in both the FCC and $L1_2$-FeCoNiV samples (Fig. 14(a, c)). The large Schmid factor and low lattice friction stress of the slip system can alleviate the intergranular incompatibility. However, an increase in the macroscopic strain creates incompatibilities and significant stress accumulation at the GBs. Therefore, several non-co-planar compatible slip systems are activated by the local accumulated stress in the FCC-FeCoNiV sample. Moreover, the activation of the compatible slip system forms a supplementary deformation substructure in the grain (Fig. 14(b)), which can adequately coordinate the intergranular deformation and release the stress accumulated at the GBs. However, because the compatible slip system driven by local stress at the GBs requires more energy to sustain slip in the grains of the $L1_2$-FeCoNiV sample, the stress accumulated at the GBs is not sufficient to motivate the formation of the deformation substructure (Fig. 14(d)). Crack initiation occurs at the GBs, which explains the appearance of intergranular fracture features in the $L1_2$-FeCoNiV HEA.

5. Conclusions

The deformation behavior in an ordered $L1_2$-structured FeCoNiV HEA was systematically investigated using the in situ EBSD/DIC method by comparing it with a disordered FCC-structured HEA. The main conclusions are as follows:

1 The in situ EBSD and DIC results show that {111}<110> slip systems were activated in the FCC/$L1_2$-structured samples, and the slip systems with maximum and secondary Schmid factors were often activated first in almost all grains. More slip systems were activated with increasing strain, and a deformation substructure gradually formed within the grains. Statistical analysis indicated that the misorientation and number of grains with the deformation substructure in the $L1_2$ sample were significantly fewer than those in the FCC sample.
2 The average angle of rotation was confirmed to increase linearly with respect to the macroscopic plastic strain for the FCC/$L1_2$-structured samples. In addition, a lower average lattice rotation rate was observed for the $L1_2$ sample than in the FCC sample, which macroscopically verified that the additional obstacles to dislocation slip caused by the ordered structure decreased the slip shear rate during plastic deformation and contributed to the high strength of the $L1_2$-FeCoNiV HEA.
3 Because the compatible slip system in the $L1_2$ sample driven by local stress at the GBs was blocked, the stress accumulated at the GBs eventually exceeded the bearing strength, leading to crack initiation at the GBs. However, these cracks did not spread rapidly owing to the lack of a driving force; therefore, the material exhibited the fracture features of dimples and intergranular fracture.

CRediT authorship contribution statement

Zhenhua Ye: Writing – original draft, Methodology, Investigation, Data curation. **Chuanwei Li:** Writing – review & editing. **Mengyao Zheng:** Methodology. **Xinyu Zhang:** Writing – review & editing. **Xudong Yang:** Data curation. **Jianfeng Gu:** Supervision,

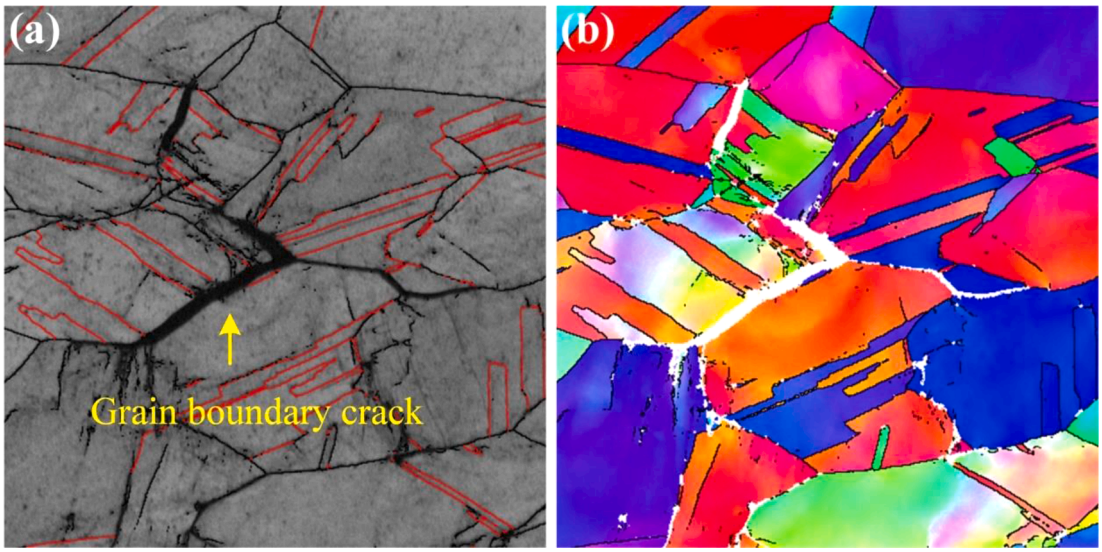

Fig. 13. (a) Morphology and (b) IPF map of a crack at a GB and the surrounding grains in the $L1_2$-FeCoNiV HEA subjected to a macroscopic plastic strain of 18%.

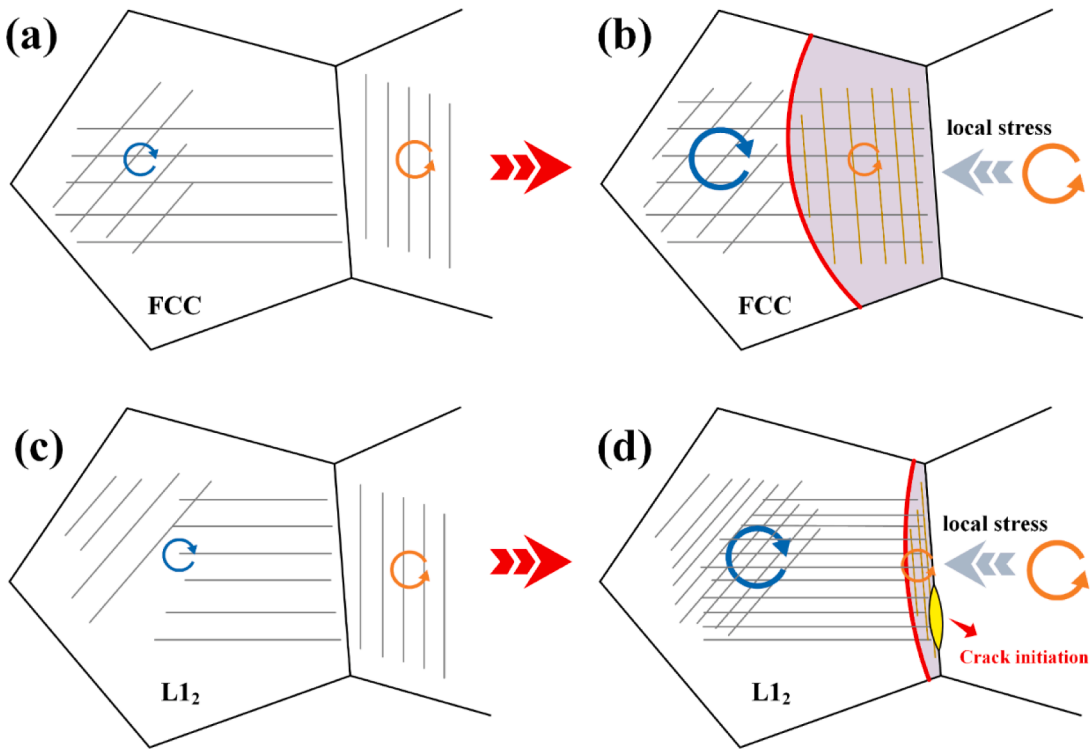

Fig. 14. Schematic illustration of deformation and fracture mechanism in the (a, b) FCC- and (c, d) $L1_2$-structured FeCoNiV HEAs.

Writing – review & editing.

Declaration of competing interest

The authors declare that they have no known competing financial interests or personal relationships that could have appeared to influence the work reported in this paper.

Acknowledgments

This work was supported by the China Postdoctoral Science Foundation (grant number 2020T130402) and the National Natural Science Foundation of China (grant number 51801126).

Appendix A

At each strain step i, the rotation matrix $\boldsymbol{R}_{s,i}$ can be defined by Euler angles as follows:

$$\boldsymbol{R}_{s,i}=\begin{bmatrix} cos\varphi_1\ cos\varphi_2-sin\varphi_1\ sin\varphi_2\ cos\Phi & -sin\varphi_2\ cos\varphi_1-cos\varphi_2\ sin\varphi_1 & sin\varphi_1\ sin\Phi \\ cos\varphi_2\ sin\varphi_1+sin\varphi_2\ cos\varphi_1\ cos\Phi & -sin\varphi_1\ sin\varphi_2+cos\varphi_1\ cos\varphi_2\ cos\Phi & -cos\varphi_2\ sin\Phi \\ sin\varphi_2\ sin\Phi & cos\varphi_2\ sin\Phi & cos\Phi \end{bmatrix} \tag{A1}$$

The lattice rotation $\boldsymbol{R}_{i,j}$ between arbitrary strain steps can be described as:

$$\boldsymbol{R}_{i,j}=\boldsymbol{E}\boldsymbol{R}_{s,j}\boldsymbol{R}_{s,i}^{-1} \tag{A2}$$

Where $\boldsymbol{E}$ is the crystal symmetrical operation for cubic structure metals (Engler and Randle, 2009). The sense of matrix $\boldsymbol{E}$ here is to eliminate the mistake caused by the crystal symmetry. Hence, the rotation angle θ between these steps is chosen as the minimum value among the 24 angles (Randle and Ralph, 1986):

$$\theta=min\left(cos^{-1}\left(\frac{R_{11}R_{22}R_{33}-1}{2}\right)\right) \tag{A3}$$

Meanwhile, the rotation axis $\boldsymbol{R}_a$ referred to crystal coordinate system is represented by

$$\boldsymbol{R}_a=\left[\frac{R_{23}-R_{32}}{2sin\theta}\ \frac{R_{13}-R_{31}}{2sin\theta}\ \frac{R_{12}-R_{21}}{2sin\theta}\right] \tag{A4}$$

Appendix B

The slip systems of FCC lattice are expressed as $\{h_ik_il_i\}\langle u_iv_iw_i\rangle$. The orientation of individual grain (j) in a reference frame (X, Y, Z) can be defined as $\{H_jK_jL_j\}\langle U_jV_jW_j\rangle$, where $[H_jK_jL_j]||$ND (normal direction of the specimen) and $[U_jV_jW_j]||$LA (loading axis). The rotation axis $\boldsymbol{R}_{as}=[r_is_it_i]$ is then calculated by Sachs model:

$$[r_is_it_i]=\left[U_jV_jW_j\right]\times[u_iv_iw_i] \tag{A5}$$

According to Rodrigues' rotation formula, rotating vector $\boldsymbol{LA}$ about $\boldsymbol{R}_{as}$ leads to an θ angle rotation of $\boldsymbol{LA}$ to $\boldsymbol{LA}^r$:

$$\boldsymbol{LA}^r=\boldsymbol{LA}\cos\theta+\boldsymbol{R}_{as}\times\boldsymbol{LA}\sin\theta+(\boldsymbol{R}_{as}\ \boldsymbol{LA})\boldsymbol{R}_{as}(1-\cos\theta) \tag{A6}$$

Through Eq. (A6), $\boldsymbol{LA}^r$ in deformed crystal coordinate system can be calculated after the assumed slip system being active, and the rotation path of the tension axis vector in crystal coordinate system can be calculated.

Appendix C

A displacement field **u**(X) provided by DIC analysis can be used to calculate the components of deformation gradient **F** associated with the in-plane deformation. The **F** can be calculated as (Di Gioacchino and Clegg, 2014):

$$F_{ij}=u_{i,j}+\delta_{ij} \tag{A7}$$

Where δ_{ij} is the Kronecker delta (i.e., $\delta_{ij}=0$ for $i\neq j$ and $\delta_{ij}=1$ for $i=j$) and the term $u_{i,j}=\partial u_i/\partial X_j$ describes the chance of the i component of displacement on an increment of distance along the direction j.

And the strain tensor for small deformation can be written as: $\varepsilon_{ij}=\frac{1}{2}(u_{i,j}+u_{i,j})$, hence, the shear on the plane investigated, $\gamma=F_{12}+F_{21}$. To consider the out of plane shear, an effective maximum shear strain γ_{max} is used to describe the distribution of plastic strain:

$$\gamma_{max}=\sqrt{\left(\frac{F_{11}-F_{22}}{2}\right)^2+\left(\frac{\gamma}{2}\right)^2} \tag{A8}$$

In addition, ω_3, representing shear generally gives rise to a material rotation can be described as:

$$\omega_3=\frac{1}{2}(F_{12}-F_{21}) \tag{A9}$$

References

Bieler, T.R., Alizadeh, R., Peña-Ortega, M., Llorca, J., 2019. An analysis of (the lack of) slip transfer between near-cube oriented grains in pure Al. Int. J. Plastic. 118, 269–290. https://doi.org/10.1016/j.ijplas.2019.02.014.

Bieler, T.R., Eisenlohr, P., Zhang, C., Phukan, H.J., Crimp, M.A., 2014. Grain boundaries and interfaces in slip transfer. Curr. Opin. Solid State Mate. Sci 18, 212–226. https://doi.org/10.1016/j.cossms.2014.05.003.

Cantor, B., Chang, I.T.H., Knight, P., Vincent, A.J.B., 2004. Microstructural development in equiatomic multicomponent alloys. Mat. Sci. Eng. A-Struct 375, 213–218. https://doi.org/10.1016/j.msea.2003.10.257.

Chen, P., Mao, S.C., Liu, Y., Wang, F., Zhang, Y.F., Zhang, Z., Han, X.D., 2013. In-situ EBSD study of the active slip systems and lattice rotation behavior of surface grains in aluminum alloy during tensile deformation. Mater. Sci. Eng.: A 580, 114–124. https://doi.org/10.1016/j.msea.2013.05.046.

Di Gioacchino, F., Clegg, W.J., 2014. Mapping deformation in small-scale testing. Acta Mater. 78, 103–113. https://doi.org/10.1016/j.actamat.2014.06.033.

Di Gioacchino, F., Quinta da Fonseca, J., 2015. An experimental study of the polycrystalline plasticity of austenitic stainless steel. Int. J. Plasticity 74, 92–109. https://doi.org/10.1016/j.ijplas.2015.05.012.

Ding, Q., Zhang, Y., Chen, X., Fu, X., Chen, D., Chen, S., Gu, L., Wei, F., Bei, H., Gao, Y., Wen, M., Li, J., Zhang, Z., Zhu, T., Ritchie, R.O., Yu, Q., 2019. Tuning element distribution, structure and properties by composition in high-entropy alloys. Nature 574, 223–227. https://doi.org/10.1038/s41586-019-1617-1.

Guan, Y., Chen, B., Zou, J., Britton, T.B., Jiang, J., Dunne, F.P.E., 2017. Crystal plasticity modelling and HR-DIC measurement of slip activation and strain localization in single and oligo-crystal Ni alloys under fatigue. Int. J. Plastic. 88, 70–88. https://doi.org/10.1016/j.ijplas.2016.10.001.

Guo, Y., Britton, T.B., Wilkinson, A.J., 2014. Slip band–grain boundary interactions in commercial-purity titanium. Acta Mater. 76, 1–12. https://doi.org/10.1016/j.actamat.2014.05.015.

He, F., Yang, Z., Liu, S., Chen, D., Lin, W., Yang, T., Wei, D., Wang, Z., Wang, J., Kai, J.-j., 2021. Strain partitioning enables excellent tensile ductility in precipitated heterogeneous high-entropy alloys with gigapascal yield strength. Int. J. Plastic. 144 https://doi.org/10.1016/j.ijplas.2021.103022.

He, J.Y., Wang, H., Huang, H.L., Xu, X.D., Chen, M.W., Wu, Y., Liu, X.J., Nieh, T.G., An, K., Lu, Z.P., 2016. A precipitation-hardened high-entropy alloy with outstanding tensile properties. Acta Mater. 102, 187–196. https://doi.org/10.1016/j.actamat.2015.08.076.

Hémery, S., Villechaise, P., 2019. In situ EBSD investigation of deformation processes and strain partitioning in bi-modal Ti-6Al-4V using lattice rotations. Acta Mater. 171, 261–274. https://doi.org/10.1016/j.actamat.2019.04.033.

Hosford, W.F., 1977. On orientation changes accompanying slip and twinning. texture of crystalline solids. 2, 175–182. https://doi.org/10.1155/tsm.2.175.

Hutchinson, J.W., 1970. Elastic-plastic behaviour of polycrystalline metals and composites. Sciences 319, 247–272. https://doi.org/10.2307/77755.

Jo, Y.H., Choi, W.M., Kim, D.G., Zargaran, A., Lee, K., Sung, H., Sohn, S.S., Kim, H.S., Lee, B.J., Lee, S., 2019. Utilization of brittle σ phase for strengthening and strain hardening in ductile VCrFeNi high-entropy alloy. Mater. Sci. Eng.: A 743, 665–674. https://doi.org/10.1016/j.msea.2018.11.136.

Joo, S.-.H., Lee, J.K., Koo, J.-.M., Lee, S., Suh, D.-.W., Kim, H.S., 2013. Method for measuring nanoscale local strain in a dual phase steel using digital image correlation with nanodot patterns. Scr. Mater. 68, 245–248. https://doi.org/10.1016/j.scriptamat.2012.10.025.

Kear, B.H., 1964. Dislocation configurations and work hardening in Cu3Au crystals. Acta Metallurgica 12, 555–569. https://doi.org/10.1016/0001-6160(64)90028-8.

Kear, B.H., 1966. Cross slip, antiphase defects and work hardening in ordered Cu3Au. Acta Metallurgica 14, 659–677. https://doi.org/10.1016/0001-6160(66)90073-3.

Lee, E.H., 1969. Elastic-plastic deformation at finite strains. J. Appl. Mech. 36, 1–6. https://doi.org/10.1115/1.3564580.

Li, J., Chen, H., Fang, Q., Jiang, C., Liu, Y., Liaw, P.K., 2020. Unraveling the dislocation–precipitate interactions in high-entropy alloys. Int. J. Plastic. 133 https://doi.org/10.1016/j.ijplas.2020.102819.

Lim, H., Carroll, J.D., Battaile, C.C., Buchheit, T.E., Boyce, B.L., Weinberger, C.R., 2014. Grain-scale experimental validation of crystal plasticity finite element simulations of tantalum oligocrystals. Int. J. Plastic. 60, 1–18. https://doi.org/10.1016/j.ijplas.2014.05.004.

Lim, H., Lee, M.G., Kim, J.H., Adams, B.L., Wagoner, R.H., 2011. Simulation of polycrystal deformation with grain and grain boundary effects. Int. J. Plastic. 27, 1328–1354. https://doi.org/10.1016/j.ijplas.2011.03.001.

Liu, C.T., 2013. Physical metallurgy and mechanical properties of ductile ordered alloys (Fe, Co, Ni)3V. Int. Metal. Rev. 29, 168–194. https://doi.org/10.1179/imtr.1984.29.1.168.

Liu, C.T., Stiegler, J.O., 1984. Ductile ordered intermetallic alloys. Science 226, 636–642. https://doi.org/10.1126/science.226.4675.636.

Liu, W.H., Lu, Z.P., He, J.Y., Luan, J.H., Wang, Z.J., Liu, B., Liu, Y., Chen, M.W., Liu, C.T., 2016. Ductile CoCrFeNiMo x high entropy alloys strengthened by hard intermetallic phases. Acta Mater. 116, 332–342. https://doi.org/10.1016/j.actamat.2016.06.063.

Margulies, L., Winther, G., Poulsen, H.F., 2001. In situ measurement of grain rotation during deformation of polycrystals. Science 291, 2392–2394. https://doi.org/10.1126/science.1057956.

McMurtrey, M.D., Was, G.S., Cui, B., Robertson, I., Smith, L., Farkas, D., 2014. Strain localization at dislocation channel–grain boundary intersections in irradiated stainless steel. Int. J. Plastic. 56, 219–231. https://doi.org/10.1016/j.ijplas.2014.01.001.

Miao, J., Pollock, T.M., Wayne Jones, J., 2009. Crystallographic fatigue crack initiation in nickel-based superalloy René 88DT at elevated temperature. Acta Mater. 57, 5964–5974. https://doi.org/10.1016/j.actamat.2009.08.022.

Mika, D.P., Dawson, P.R., 1998. Effects of grain interaction on deformation in polycrystals. Mater. Sci. Eng.: A 257, 62–76. https://doi.org/10.1016/s0921-5093(98)00824-7.

Perrin, C., Berbenni, S., Vehoff, H., Berveiller, M., 2010. Role of discrete intragranular slip on lattice rotations in polycrystalline Ni: experimental and micromechanical studies. Acta Mater. 58, 4639–4649. https://doi.org/10.1016/j.actamat.2010.04.033.

Qiu, Y., Hu, Y.J., Taylor, A., Styles, M.J., Marceau, R.K.W., Ceguerra, A.V., Gibson, M.A., Liu, Z.K., Fraser, H.L., Birbilis, N., 2017. A lightweight single-phase AlTiVCr compositionally complex alloy. Acta Mater. 123, 115–124. https://doi.org/10.1016/j.actamat.2016.10.037.

Randle, V., Ralph, B., 1986. A practical approach to the determination of the crystallography of grain boundaries. J. Mater. Sci. 21, 3823–3828. https://doi.org/10.1007/bf02431617.

Reddy, G.B., Kapoor, R., Sarkar, A., 2019. Probability based ranking approach for twin variant selection in an α-Zr alloy. Int. J. Plastic. 122, 164–187. https://doi.org/10.1016/j.ijplas.2019.06.015.

Rogal, L., Bobrowski, P., Kormann, F., Divinski, S., Stein, F., Grabowski, B., 2017. Computationally-driven engineering of sublattice ordering in a hexagonal AlHfScTiZr high entropy alloy. Sci. Rep. 7, 2209. https://doi.org/10.1038/s41598-017-02385-w.

Scheriau, S., Pippan, R., 2008. Influence of grain size on orientation changes during plastic deformation. Mater. Sci. Eng.: A 493, 48–52. https://doi.org/10.1016/j.msea.2007.08.092.

Shi, P., Li, R., Li, Y., Wen, Y., Zhong, Y., Ren, W., Shen, Z., Zheng, T., Peng, J., Liang, X., Hu, P., Min, N., Zhang, Y., Ren, Y., Liaw, P.K., Raabe, D., Wang, Y.D., 2021. Hierarchical crack buffering triples ductility in eutectic herringbone high-entropy alloys. Science 373, 912–918. https://doi.org/10.1126/science.abf6986.

Stinville, J.C., Vanderesse, N., Bridier, F., Bocher, P., Pollock, T.M., 2015. High resolution mapping of strain localization near twin boundaries in a nickel-based superalloy. Acta Mater. 98, 29–42. https://doi.org/10.1016/j.actamat.2015.07.016.

Tang, A., Liu, H., Liu, G., Zhong, Y., Wang, L., Lu, Q., Wang, J., Shen, Y., 2020. Lognormal distribution of local strain: a universal law of plastic deformation in material. Phys. Rev. Lett. 124, 155501 https://doi.org/10.1103/PhysRevLett.124.155501.

Tasan, C.C., Hoefnagels, J.P.M., Diehl, M., Yan, D., Roters, F., Raabe, D., 2014. Strain localization and damage in dual phase steels investigated by coupled in-situ deformation experiments and crystal plasticity simulations. Int. J. Plastic. 63, 198–210. https://doi.org/10.1016/j.ijplas.2014.06.004.

Tong, Y., Chen, D., Han, B., Wang, J., Feng, R., Yang, T., Zhao, C., Zhao, Y.L., Guo, W., Shimizu, Y., Liu, C.T., Liaw, P.K., Inoue, K., Nagai, Y., Hu, A., Kai, J.J., 2019. Outstanding tensile properties of a precipitation-strengthened FeCoNiCrTi0.2 high-entropy alloy at room and cryogenic temperatures. Acta Mater. 165, 228–240. https://doi.org/10.1016/j.actamat.2018.11.049.

Wang, J., Beyerlein, I.J., Tomé, C.N., 2014. Reactions of lattice dislocations with grain boundaries in Mg: implications on the micro scale from atomic-scale calculations. Int. J. Plastic. 56, 156–172. https://doi.org/10.1016/j.ijplas.2013.11.009.

Wang, S., Chen, S., Jia, Y., Hu, Z., Huang, H., Yang, Z., Dong, A., Zhu, G., Wang, D., Shu, D., Tian, F., Dai, Y., Sun, B., 2019. FCC-L12 ordering transformation in equimolar FeCoNiV multi-principal element alloy. Mater. Des 168, 107648. https://doi.org/10.1016/j.matdes.2019.107648.

Winther, G., 2008. Slip systems extracted from lattice rotations and dislocation structures. Acta Mater. 56, 1919–1932. https://doi.org/10.1016/j.actamat.2007.12.026.

Yang, T., Zhao, Y.L., Li, W.P., Yu, C.Y., Luan, J.H., Lin, D.Y., Fan, L., Jiao, Z.B., Liu, W.H., Liu, X.J., Kai, J.J., Huang, J.C., Liu, C.T., 2020. Ultrahigh-strength and ductile superlattice alloys with nanoscale disordered interfaces. Science 369, 427–432. https://doi.org/10.1126/science.abb6830.

Yang, T., Zhao, Y.L., Tong, Y., Jiao, Z.B., Wei, J., Cai, J.X., Han, X.D., Chen, D., Hu, A., Kai, J.J., Lu, K., Liu, Y., Liu, C.T., 2018. Multicomponent intermetallic nanoparticles and superb mechanical behaviors of complex alloys. Science 362, 933–937. https://doi.org/10.1126/science.aas8815.

Yeh, J.W., Chen, S.K., Lin, S.J., Gan, J.Y., Chin, T.S., Shun, T.T., Tsau, C.H., Chang, S.Y., 2004. Nanostructured high-entropy alloys with multiple principal elements: novel alloy design concepts and outcomes. Adv Eng Mater 6, 299–303. https://doi.org/10.1002/adem.200300567.

Zhao, Y.L., Yang, T., Tong, Y., Wang, J., Luan, J.H., Jiao, Z.B., Chen, D., Yang, Y., Hu, A., Liu, C.T., Kai, J.J., 2017. Heterogeneous precipitation behavior and stacking-fault-mediated deformation in a CoCrNi-based medium-entropy alloy. Acta Mater. 138, 72–82. https://doi.org/10.1016/j.actamat.2017.07.029.